The kinetics and optimality of influenza A virus locomotion

Siddhansh Agarwal,[1,2] Boris Veytsman,[3,4] Daniel A. Fletcher,[1,2] and Greg Huber[2]

[1] *Department of Bioengineering, University of California, Berkeley*
[2] *Chan Zuckerberg Biohub — San Francisco, 499 Illinois Street, San Francisco, CA 94158, USA*
[3] *Chan Zuckerberg Initiative, Redwood City, CA 94063, USA*
[4] *School of Systems Biology, George Mason University, Fairfax, VA 22030, USA*

(Dated: May 6, 2024)

Influenza A viruses (IAVs) must navigate through a dense extracellular mucus to infect airway epithelial cells. The mucous layer, composed of glycosylated biopolymers (mucins), presents sialic acid that binds to ligands on the viral envelope and can be irreversibly cleaved by viral enzymes. It was recently discovered that filamentous IAVs exhibit directed, persistent motion along their long axis on sialic acid-coated surfaces. This study demonstrates, through stochastic simulations and mean-field theory, how IAVs harness a 'burnt-bridge' Brownian ratchet mechanism for directed, persistent translational motion. We show viruses occupy the optimal parameter range ('Goldilocks zone') for efficient mucous transport, possibly due to the evolutionary adaptation of enzyme kinetics. Our findings suggest novel therapeutic targets and provide insight into possible mechanisms of zoonotic transmission.

Introduction. The onset of many infectious diseases hinges crucially on the ability of invading pathogens to traverse the extracellular environment on the way to the host cell membrane [1, 2]. Mucotropic viruses such as influenza A, must overcome the extracellular mucosal barrier protecting airway epithelial cells [3]. Despite extensive studies on the biochemistry of virus-host interactions [4, 5], a quantitative understanding of how viruses move through material barriers remains incomplete.

The mucous layer coating respiratory epithelia, with a thickness ranging from $\sim 1\,\mu$m to $10\,\mu$m [6–8], poses a critical barrier for influenza A viruses (IAVs) to overcome. Mucins have abundant binding sites for the IAV surface protein hemagglutinin (HA), effectively immobilizing viruses within the layer. Coordinated beating of cilia on epithelial cells promotes a net mucous flow resulting in clearance of pathogens before they can reach the vulnerable substrate [9–12]. With the estimated mucociliary clearance rates of $\sim 1\,$cm/min [13, 14], IAVs have a time window of just $t_c \sim 20\,$min [15] before being cleared from the airway. Clinical isolates of IAVs typically have elongated, filamentous morphologies with a cylindrical diameter between 70 nm to 90 nm and a broad length distribution ranging from 100 nm to over $5\,\mu$m [16, 17]. Shorter filamentous strands with axial lengths under 300 nm are thought to be the primary vectors spreading infection between cells [15, 18, 19]. For a virion with these dimensions, the timescale to move a distance of $\sim 10\,\mu$m based on passive diffusion alone is $t_d \sim 2\,$h. Thus the fraction of IAVs that overcome the mucous barrier is $\sim \exp(-t_d/t_c) = 2.5 \times 10^{-3}$. This is not the only defense mechanism of the host: epithelial cell surfaces in the periciliary layer beneath the layer of mucus have long, densely packed glycoprotein "brush" elements creating a steric barrier that viruses must penetrate [20, 21], further reducing the number of viruses that can reach the airway epithelium. Thus, viruses with purely diffusive motion have little chance to penetrate the mucociliary layer before being cleared away.

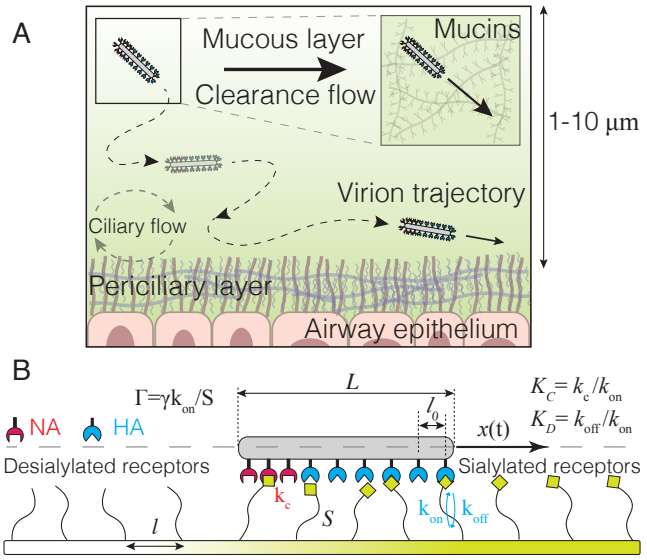

FIG. 1. (a) A virion (not to scale) navigates the complex heterogeneous and flowing mucous layer (1–10 µm) composed of highly glycosylated, entangled mucin fibers. (b) Coarse-grained model of a virion as a rigid elongated shell, positioned at a constant offset above a 1D substrate consisting of uniformly coated glycoproteins decorated with SA receptors. HA can form reversible bonds with SA on the surface, while NA cleaves these receptors irreversibly. An HA–SA bond is modeled as a Hookean spring with stiffness S, modeling the finite extensibility of the glycoproteins.

Vahey and Fletcher [15] discovered a key strategy used by IAVs to navigate host barriers: persistent movement powered by its local environment. Optical microscopy of filamentous IAVs revealed that the distribution of the proteins HA and Neuraminidase (NA) on the viral surface is polarized: NA enzyme clusters preferentially as-

sociated with the genome-containing end. Experiments on coverslips functionalized with sialic acid (SA) showed persistent translational motion of the virions away from the NA-rich pole, operating via a 'burnt-bridge' Brownian ratchet mechanism [22]. Recent work [23] has revealed that this motion is modulated by the HA/NA activity and their spatial organization, with observed differences in transport speeds and gaits, though the explored parameter space was limited. In contrast, influenza C viruses exhibit rolling motion on SA-functionalized surfaces due to the coordinated SA binding/cleavage cycle of their hemagglutinin-esterase-fusion glycoprotein [24], which imposes a uniform surface distribution of binders & cleavers. For IAVs, the elongated morphology and spatial segregation of HA and NA likely favor translational over rotational modes within native viscoelastic mucinous networks, where pore sizes (~ 100 nm) [25] impose constraints on large-scale rotational modes.

This work examines the translational motion of short filamentous IAVs, with a focus on the "delicate balance" of HA/NA activities hypothesized as a key factor governing their movement [26]. We demonstrate that in our model, due to the irreversible SA-cleaving process, the virions move with constant speed, and this speed exhibits a maximum within a specific range of HA and NA parameter values approximating those of real viruses. This suggests that evolutionary pressures may have selected for viruses optimized to enhance their ability to navigate and penetrate host barriers.

Model. We map the 3D trajectory of a virion onto an effective 1D track in the reference frame of the virus particle. This model captures the essential physics while remaining computationally tractable. We consider a coarse-grained representation of an IAV as a rigid, 1D rod of length L ($\sim 300\,$nm). The viral envelope is populated by a distributed array of HA spikes engaged in binding SA moieties, and NA enzyme complexes which cleave these receptors. Typical mean separations between HA on the IAV envelope are $l_0 \sim 10$ nm ($l_0 \ll L$). Thus, we assume there are 30 ligands distributed uniformly on the simulated virus surface.

We model the virus as positioned at a fixed elevation above a 1D substrate uniformly decorated with SA at an average spacing $l \sim 2.5\,$nm reflecting typical glycoprotein densities. HA binding to SA is described as a bimolecular reaction with the off-rate ($k_{\rm off}$) from empirical measurements [27], and the on-rate ($k_{\rm on}$) estimated by modeling HA trimers and SA as confined complexes following previous studies [15, 23]. NA irreversibly cleaves HA-bound SA via first-order kinetics with a catalytic rate k_c [28]. HA-SA interactions are represented as Hookean springs accounting for glycoprotein linker flexibility [24], coarse-graining fast fluctuations while capturing effective entropic elasticity. In the following, we choose l_0 and $k_{\rm on}$ as the length and inverse time scales, respectively, with specific parameter values provided in the Supplementary Material (SM).

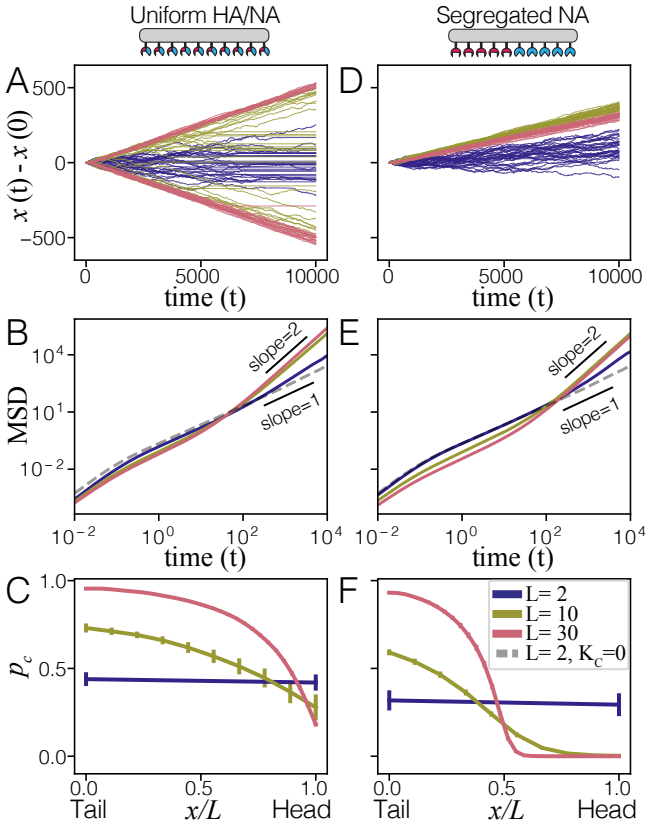

FIG. 2. IAV locomotion with uniform (A-C) versus segregated (D-F) HA/NA distributions for different virus lengths L. Displacement from the initial position $x(t) - x(0)$ plotted against time t demonstrates SSB for uniform HA/NA distribution (A), while the virus consistently moves away from the NA pole for the segregated case (D). (B, E) Mean-squared displacement (MSD) versus time plots show the transition from diffusive (slope = 1) to ballistic motion (slope = 2) as L increases. (C, F) The averaged SA cleavage probabilities along the virus x/L highlight the distinct SA cleavage profiles and consequent directional biases between the two HA/NA distributions.

We scale the rates of bond formations and cleaving by $\exp(-u/(k_BT)) = \exp(-\Delta x^2/\alpha^2)$, where u is the potential energy of the spring stretched by the value Δx, and $\alpha = \sqrt{2k_BT/(Sl_0^2)}$ is the characteristic length under thermal fluctuations. The dimensionless binding/unbinding rates $q_{\rm off} = K_D/(1 + \exp(-\Delta x^2/\alpha^2))$, $q_{\rm on} = \exp(-\Delta x^2/\alpha^2)/(1 + \exp(-\Delta x^2/\alpha^2)$ are given by transition-state theory (see, e.g., [29]), defining an effective stretch-dependent dissociation constant $q_{\rm off}/q_{\rm on} = K_D \exp(\Delta x^2/\alpha^2)$, where $K_D = k_{\rm off}/k_{\rm on}$. The dimensionless NA cleavage rate is $q_c = K_C \exp(-\Delta x^2/\alpha^2)$, where $K_C = k_c/k_{\rm on}$. In the simulations we use overdamped dynamics, excluding the explicit thermal noise:

$$v = -\frac{1}{\Gamma L}\sum_i \Delta x_i,\; v = dx(t)/dt, \qquad (1)$$

where $\Gamma = \gamma k_{\rm on}/S$ is the ratio of spring relaxation to bond formation timescales and represents the friction coefficient per unit length. In contrast to conventional Langevin dynamics, the thermal noise term is omitted in our analysis, since $1/(\Gamma L) \gg \sqrt{2k_BT/(\gamma k_{\rm on} l_0)}$, indicating that the spring forces predominate over higher-frequency thermal fluctuations. At each time step, we first stochastically update the configuration of bound springs and cleaved receptors via Gillespie algorithm, an efficient kinetic Monte Carlo approach [30, 31]. Then the net instantaneous force is computed and used to update the velocity and position of the virus in (1).

This insight, that the most important process in the system is the formation, arrangement and cleavage of the bonds, is the key for the analytical treatment. We assume the large separation of time scales between binding/unbinding, on one hand, and cleavage together with virus motion, on another hand. Thus at any time and location, the configuration of bonds is close to the equilibrium one, and we calculate its Gibbs free energy G summing the logs of partition functions of bonds formed at each virus site (see the SM for details). When the number of virus sites is large, we can use the continuous limit, and the sum becomes the integral,

$$G = -\frac{k_BT}{l}\int_0^L \log\left[\frac{(K_D + \sqrt{\pi}(1-p_c)\alpha l_0/l)}{K_D}\right]dx, \quad (2)$$

where $p_c(x)$ is the probability that a substrate site is burned. If the virus moves with a constant speed v, the cleaving probability profile $p_c(t,x)$ satisfies the steady state equation,

$$\frac{\partial p_c}{\partial t} - v\frac{\partial p_c}{\partial x} = 0. \quad (3)$$

Differentiating equation (2) by time and using equation (3), we can calculate the production of free energy dG/dt.

Free energy produced by the irreversible cleaving dissipates through the friction of the virus as a whole and friction due to bonds "snapping" [32]. Equating free-energy production to dissipation when the virus moves with a steady speed v, we get

$$\frac{dG}{dt} = \gamma L v^2 + \frac{Sv^2}{2k_{\rm off}}\int_0^L p_b(x)dx, \quad (4)$$

where $p_b(x) = \sqrt{\pi}(1-p_c)\alpha(l_0/l)/(K_D+\sqrt{\pi}(1-p_c)\alpha l_0/l)$ is the binding probability. See the SM for further details of the simulations and analytical calculations.

Results and Discussion. For simplicity, we discuss only two configurations of binders and cleavers on the viral envelope: (i) a uniform distribution of HA and NA over the virion's surface, and (ii) a spatially segregated case where NA is localized to half of the virion, while HA is uniformly distributed. For the uniform case (Fig. 2A–C),

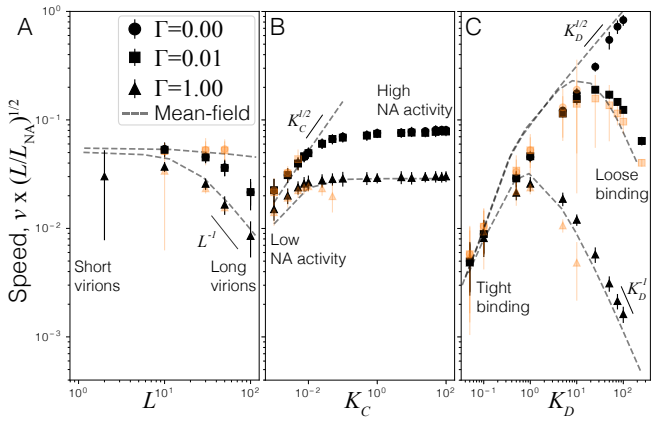

FIG. 3. IAV motion varies with HA/NA activity and Γ. (A) Speed (v) versus virus length (L) shows SSB above a threshold L for the uniform case (orange), with $v \sim L^{-1}$ for long L; ($K_C = 0.075$, $K_D = 1$). (B) v versus K_C indicates blocked motion beyond $K_C \approx 0.5$ for a uniform distribution (orange), while the asymmetric case (black) exhibits a persistent K_C-independent v; ($L = 30$, $K_D = 1$). (C) v versus K_D reveals an optimal K_D, shifting right with decreasing Γ; ($L = 30$, $K_C = 0.075$). Markers denote different Γ values for uniform (orange) and asymmetric (black) cases; dashed lines are speeds from mean-field theory.

increasing viral length L triggers a spontaneous symmetry breaking (SSB) transition from diffusive motion (purple, $L = 2$) to ballistic, directional motion (red, $L = 30$). The mean-squared displacement (MSD) vs time (Fig. 2B) clearly shows this transition: the long-time MSD exponent approaches 2 as L increases. The symmetry breaking arises spontaneously from stochastic, differential NA-mediated cleavage of SA receptors across the virus length, despite the initial HA/NA symmetry. The resulting self-generated SA gradients prompt chemotactic migration, a striking behavior emerging from simple, uncoordinated HA/NA-SA interactions.

In the segregated NA case (Fig. 2D–F) the symmetry is absent, and the virion robustly propels away from the NA-rich side at any L. This built-in polarity facilitates a much faster transition to ballistic motion as L increases (Fig. 2E). The diffusive, non-cleaving case ($L = 2$, $K_C = 0$, dashed gray) is shown for reference. Analyzing steady-state cleaved SA profiles beneath the virus (Fig. 2C, F) reveals the mechanisms of the ballistic motion: For uniform HA/NA, a head-tail gradient develops spontaneously despite the initial symmetry, but requires a critical virus length $L \sim 10$ to fully establish SSB. Conversely, the segregated case inherently generates a robust concentration gradient due to asymmetric NA distribution. We note that the viruses in our model resemble active Brownian particles that move with constant speed, slowly changing direction or turning when bumping into obstacles [33].

Analytical theory provides a quantitative framework to

understand the steady-state cleaving profile p_c along the virus length x/L obtained from simulations in Figs. 2C,F. The mean-field gradient length scale arising from cleaving is given by,

$$L_c = l_0\sqrt{\frac{\alpha}{\sqrt{\pi}K_C}}. \tag{5}$$

For the locomotion to occur, L_c must satisfy the condition $l_0 < L_c < L$, where l_0 is the substrate receptor spacing and L is the virus length. Above the virus length L, the gradient is too shallow, rendering the binding landscape effectively uniform from the particle's perspective. Below l_0 the gradient is too steep, cleaving all receptor sites and detaching the virus from the substrate.

Figure 3 shows details of the viral locomotion as the function of the parameters: length L, NA catalytic activity K_C, HA-SA dissociation constant K_D, and friction Γ. The long-time MSD data for trajectories (e.g. Figs. 2B,E) is fitted to obtain the speed v. For both uniform and segregated HA/NA distributions, a minimal virus length $L > L_c \approx 10$ is required to establish ballistic motion (Fig. 3A). As ΓL becomes larger, the speed v scales as L^{-1}, in agreement with the analytical computations. Thus larger virions move more slowly through "sticky" environments.

However, the role of the NA cleavage activity K_C (Fig. 3B) is strikingly different in the uniform and the segregated cases. For the uniform case, the predicted range for K_C from mean-field analysis is $\alpha l_0^2/(\sqrt{\pi}L^2) \ll K_C \ll \alpha/\sqrt{\pi}$, which for our parameters reads $10^{-3} \ll K_C \ll 0.5$. Indeed, v abruptly drops to zero beyond a threshold $K_C \gtrsim 0.5$ (orange points), cleaving all available substrate sites and forbidding SSB. In contrast, the segregated case maintains robust motion even at high K_C, approaching a constant terminal v. This demonstrates how spatial segregation allows a lower limit on L_c, conferring resilience against fluctuations in NA activity.

Remarkably, v exhibits a non-monotonic dependence on K_D (Fig. 3C), with an optimal intermediate K_D maximizing the speed. Conditions of both tight (low K_D) *and* loose (high K_D) binding result in hindered motion, with the respective origins being excessive bond friction and insufficient driving force. This defines a 'Goldilocks' constraint on K_D. Mean-field analysis allows us to estimate the optimal K_D as

$$K_{D,\mathrm{opt}} = \frac{1}{\sqrt{2}} + 2\alpha\left(\frac{\sqrt{\pi}l_0^4}{K_C l^2\Gamma^2 L^2}\right)^{1/3}. \tag{6}$$

In the $\Gamma L \to 0$ limit, the optimal K_D systematically increases as $(\Gamma L)^{-2/3}$, going to ∞ as, in this regime, minimizing bond friction dominates. In the $\Gamma L \to \infty$ limit, it goes to the constant value of $1/\sqrt{2}$. Thus, small changes in K_D or ΓL can give rise to markedly different transport speeds, whereas the catalytic rate K_C has a relatively minor effect.

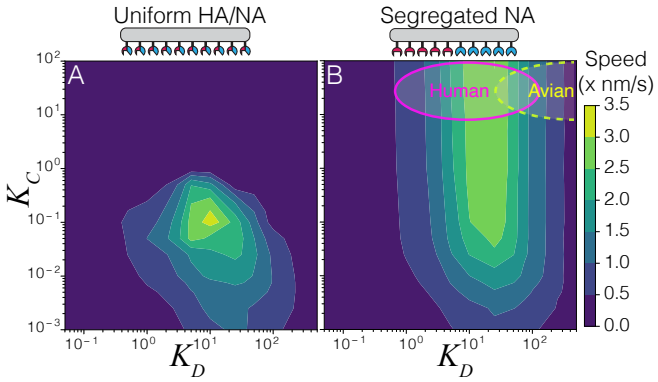

FIG. 4. Speed heatmaps of IAV ($L = 30$, $\Gamma = 0.01$) as a function of HA-SA dissociation constant (K_D) and NA-SA cleavage rate (K_C). For uniform HA/NA distribution (A), motion is confined to a narrow zone where K_D and K_C must be precisely tuned for efficient movement. In contrast, the polarised case (B) exhibits an extended mobile regime, indicating spatial segregation broadens the 'Goldilocks zone' of optimal transport. Magenta outline: Range of K_D and K_C values for human IAV strains binding to/cleaving α2,6Sia in the human upper respiratory tract. Yellow dashed outline: Approximate K_D and K_C values for avian IAV strains binding to/cleaving α2,6Sia.

Figure 4 maps the steady state speed in the parameter space of HA-SA dissociation constant (K_D) and NA cleavage activity (K_C). We choose $\Gamma = 10^{-2}$ as physiologically relevant for IAVs navigating native mucinous environments, whose bulk viscosity can be much greater than that of water [34]. The heatmap shows different transport landscapes for uniform and polarized distributions. For the uniform case (Fig. 4A), effective movement is restricted to a narrow zone. In contrast, for the segregated case (Fig. 4B), an expansive high-speed regime spans a broad range of K_D and K_C, indicating an inherent robustness conferred by asymmetric protein distribution on the viral envelope.

We show in Fig. 4B the estimated parameter ranges for human IAV strains binding to/catalyzing the α2,6-linked sialic acid (α2,6Sia) found in humans [35]. The measured K_D and K_C rates [27, 28, 36] lie within an optimal region (magenta) predicted by the model (see SM for details). While kinetic data for single HA-α2,6Sia bonds of avian IAV strains is lacking, the ∼10x higher K_D value for α2,6Sia binding [37] corresponds to a distinct optimal cluster on the contour plot (yellow dashed outline), reflecting evolutionary adaptations to preferentially bind avian α2,3Sia receptors [38, 39]. Interestingly, retrospective analyses show historical pandemic precursor IAV strains acquired incremental HA mutations enhancing affinity for α2,6Sia receptors [40], a critical adaptation increasing human-to-human transmissibility. Furthermore, the presence of both α2,3Sia and α2,6Sia linkages in pigs allows them to serve as "mixing vessels" that facilitate IAV reassortment [41]. Thus, our framework provides a

quantitative basis to understand how IAV receptor binding specificities contribute to host tropism and zoonotic transmission risk.

Our model also suggests that targeting IAV transport could be a useful antiviral strategy. While NA inhibitors (NAIs) like zanamivir and oseltamivir (Tamiflu) can reduce NA activity [42], our model shows that IAV locomotion is largely insensitive to NA activity. A dramatic shift along K_C axis is required to significantly block motion—which may contribute to the limited efficacy of NAIs in treating influenza [43, 44]. In contrast, we predict the HA-SA K_D to be a particularly attractive target for antivirals, as modest changes in on-rate or off-rate could more effectively move IAV out of the 'Goldilocks zone' required for directed motion.

Conclusions. The rich phenomenological behavior of IAV locomotion stems from the interplay of stochastic receptor-ligand kinetics with dissipative mechanics governing motion in viscous environments. The existence of an optimal receptor-ligand binding-affinity range, finely tuned to the ambient viscosity, highlights a fundamental trade-off—overly tight binding hinders transport via excessive frictional forces, while loose binding forbids the transient receptor-ligand interactions required for motion. IAV locomotion hinges on a delicate balance between HA binding strength, NA cleavage activity, their spatial distribution on the virion surface, and the properties of the microenvironment. We find that segregating NA activity confers resilience, enabling robust directed movement across a broad range of receptor affinities and an even broader range of cleavage rates.

Our work identifies the molecular design principles important for a viral nanotransport strategy, insights that can be extended to many engineered systems [45–49]. Fundamentally, IAV-envelope organization appears engineered to leverage stochastic multivalent receptor-ligand kinetics for directed locomotion. The remarkable correspondence between the properties of IAVs and efficient transport across the epithelial barrier highlights this host defense as a critical evolutionary bottleneck. Viruses experience immense selective pressure to overcome multiple layers of host defenses and successfully infect target cells. Our findings show that locomotion through the mucociliary layer is an important source of evolutionary pressure. Since the optimal parameters differ across host species, mutations enabling zoonotic transmission must confer enhanced movement within the mucosal environment. Disrupting the balance between virion adhesive kinetics and mechanics may present opportunities for new antivirals that subvert this key aspect of influenza's evolutionary prowess. Taken together, our findings could catalyze development of next-generation therapies specifically targeting influenza's envelope organization and directed-locomotion strategy.

Acknowledgements. We thank Guillaume Le Treut, David Yllanes, Amy Kistler and Michael Vahey for helpful discussions and suggestions. We thank CZ Biohub—SF and CZ Science for generous support.

[1] L. E. Wallace, M. Liu, F. J. van Kuppeveld, E. de Vries, and C. A. de Haan, Respiratory mucus as a virus-host range determinant, Trends in Microbiology **29**, 983 (2021).
[2] A. S. Mall, H. Habte, Y. Mthembu, J. Peacocke, and C. De Beer, Mucus and mucins: do they have a role in the inhibition of the human immunodeficiency virus?, Virology journal **14**, 1 (2017).
[3] K. S. LeMessurier, M. Tiwary, N. P. Morin, and A. E. Samarasinghe, Respiratory barrier as a safeguard and regulator of defense against influenza a virus and streptococcus pneumoniae, Frontiers in immunology **11**, 512250 (2020).
[4] M. Koehler, M. Delguste, C. Sieben, L. Gillet, and D. Alsteens, Initial step of virus entry: virion binding to cell-surface glycans, Annual review of virology **7**, 143 (2020).
[5] N. L. Miller, T. Clark, R. Raman, and R. Sasisekharan, Glycans in virus-host interactions: A structural perspective, Frontiers in Molecular Biosciences **8**, 666756 (2021).
[6] D. B. Hill, B. Button, M. Rubinstein, and R. C. Boucher, Physiology and pathophysiology of human airway mucus, Physiological Reviews **102**, 1757 (2022).
[7] G. C. Hansson, Mucus and mucins in diseases of the intestinal and respiratory tracts, Journal of internal medicine **285**, 479 (2019).
[8] O. W. Williams, A. Sharafkhaneh, V. Kim, B. F. Dickey, and C. M. Evans, Airway mucus: from production to secretion, American journal of respiratory cell and molecular biology **34**, 527 (2006).
[9] S. K. Lai, Y.-Y. Wang, D. Wirtz, and J. Hanes, Micro- and macrorheology of mucus, Advanced drug delivery reviews **61**, 86 (2009).
[10] J. V. Fahy and B. F. Dickey, Airway mucus function and dysfunction, New England Journal of Medicine **363**, 2233 (2010).
[11] B. Button, L.-H. Cai, C. Ehre, M. Kesimer, D. B. Hill, J. K. Sheehan, R. C. Boucher, and M. Rubinstein, A periciliary brush promotes the lung health by separating the mucus layer from airway epithelia, Science **337**, 937 (2012).
[12] G. R. Ramirez-San Juan, A. J. T. M. Mathijssen, M. He, L. Jan, W. Marshall, and M. Prakash, Multi-scale spatial heterogeneity enhances particle clearance in airway ciliary arrays, bioRxiv 10.1101/665125 (2019).
[13] J. A. Voynow and B. K. Rubin, Mucins, mucus, and sputum, Chest **135**, 505 (2009).
[14] X. M. Bustamante-Marin and L. E. Ostrowski, Cilia and mucociliary clearance, Cold Spring Harbor perspectives in biology **9**, a028241 (2017).
[15] M. D. Vahey and D. A. Fletcher, Influenza A virus surface proteins are organized to help penetrate host mucus, Elife **8**, e43764 (2019).
[16] D. P. Nayak, R. A. Balogun, H. Yamada, Z. H. Zhou, and S. Barman, Influenza virus morphogenesis and budding, Virus research **143**, 147 (2009).
[17] P. Chlanda, O. Schraidt, S. Kummer, J. Riches, H. Oberwinkler, S. Prinz, H.-G. Kräusslich, and J. A. Briggs,

Structural analysis of the roles of influenza a virus membrane-associated proteins in assembly and morphology, Journal of virology **89**, 8957 (2015).

[18] T. Li, Z. Li, E. E. Deans, E. Mittler, M. Liu, K. Chandran, and T. Ivanovic, The shape of pleomorphic virions determines resistance to cell-entry pressure, Nature microbiology **6**, 617 (2021).

[19] S. Vijayakrishnan, C. Loney, D. Jackson, W. Suphamungmee, F. J. Rixon, and D. Bhella, Cryotomography of budding influenza a virus reveals filaments with diverse morphologies that mostly do not bear a genome at their distal end, PLoS pathogens **9**, e1003413 (2013).

[20] E. Puchelle, S. De Bentzmann, and J. Zahm, Physical and functional properties of airway secretions in cystic fibrosis-therapeutic approaches, Respiration **62**, 2 (1995).

[21] M. King, Physiology of mucus clearance, Paediatric respiratory reviews **7**, S212 (2006).

[22] J. Mai, I. Sokolov, and A. Blumen, Directed particle diffusion under "burnt bridges" conditions, Physical Review E **64**, 011102 (2001).

[23] L. Stevens, S. de Buyl, and B. M. Mognetti, The sliding motility of the bacilliform virions of Influenza A viruses, Soft matter **19**, 4491 (2023).

[24] F. Ziebert and I. M. Kulić, How influenza's spike motor works, Physical Review Letters **126**, 218101 (2021).

[25] B. S. Schuster, J. S. Suk, G. F. Woodworth, and J. Hanes, Nanoparticle diffusion in respiratory mucus from humans without lung disease, Biomaterials **34**, 3439 (2013).

[26] E. de Vries, W. Du, H. Guo, and C. A. de Haan, Influenza a virus hemagglutinin–neuraminidase–receptor balance: Preserving virus motility, Trends in microbiology **28**, 57 (2020).

[27] J. L. Cuellar-Camacho, S. Bhatia, V. Reiter-Scherer, D. Lauster, S. Liese, J. P. Rabe, A. Herrmann, and R. Haag, Quantification of multivalent interactions between sialic acid and influenza A virus spike proteins by single-molecule force spectroscopy, Journal of the American Chemical Society **142**, 12181 (2020).

[28] D. J. Benton, S. R. Martin, S. A. Wharton, and J. W. McCauley, Biophysical measurement of the balance of Influenza A hemagglutinin and neuraminidase activities, Journal of Biological Chemistry **290**, 6516 (2015).

[29] S. Marbach and C. E. Miles, Coarse-grained dynamics of transiently bound fast linkers, The Journal of Chemical Physics **158** (2023).

[30] D. T. Gillespie, A general method for numerically simulating the stochastic time evolution of coupled chemical reactions, Journal of Computational Physics **22**, 403 (1976).

[31] D. T. Gillespie, Exact stochastic simulation of coupled chemical reactions, The Journal of Physical Chemistry **81**, 2340 (1977).

[32] P. Sens, Rigidity sensing by stochastic sliding friction, EPL (Europhysics Letters) **104**, 38003 (2013).

[33] M. C. Marchetti, Y. Fily, S. Henkes, A. Patch, and D. Yllanes, Minimal model of active colloids highlights the role of mechanical interactions in controlling the emergent behavior of active matter, Current Opinion in Colloid & Interface Science **21**, 34 (2016).

[34] S. K. Lai, Y.-Y. Wang, D. Wirtz, and J. Hanes, Micro- and macrorheology of mucus, Advanced drug delivery reviews **61**, 86 (2009).

[35] P. Gagneux, M. Cheriyan, N. Hurtado-Ziola, E. C. B. van der Linden, D. Anderson, H. McClure, A. Varki, and N. M. Varki, Human-specific regulation of α2–6-linked sialic acids, Journal of Biological Chemistry **278**, 48245 (2003).

[36] D. K. Takemoto, J. J. Skehel, and D. C. WILEY, A surface plasmon resonance assay for the binding of influenza virus hemagglutinin to its sialic acid receptor, Virology **217**, 452 (1996).

[37] X. Xiong, P. J. Coombs, S. R. Martin, J. Liu, H. Xiao, J. W. McCauley, K. Locher, P. A. Walker, P. J. Collins, Y. Kawaoka, *et al.*, Receptor binding by a ferret-transmissible h5 avian influenza virus, Nature **497**, 392 (2013).

[38] T. P. Peacock, D. J. Benton, J.-R. Sadeyen, P. Chang, J. E. Sealy, J. E. Bryant, S. R. Martin, H. Shelton, J. W. McCauley, W. S. Barclay, *et al.*, Variability in h9n2 haemagglutinin receptor-binding preference and the ph of fusion, Emerging microbes & infections **6**, 1 (2017).

[39] S.-J. Richards, A. N. Baker, M. Walker, and M. I. Gibson, Polymer-stabilized sialylated nanoparticles: Synthesis, optimization, and differential binding to influenza hemagglutinins, Biomacromolecules **21**, 1604 (2020).

[40] M. Liu, A. S. Bakker, Y. Narimatsu, F. J. van Kuppeveld, H. Clausen, C. A. de Haan, and E. de Vries, H3n2 influenza a virus gradually adapts to human-type receptor binding and entry specificity after the start of the 1968 pandemic, Proceedings of the National Academy of Sciences **120**, e2304992120 (2023).

[41] M. Liu, F. J. van Kuppeveld, C. A. de Haan, and E. de Vries, Gradual adaptation of animal influenza a viruses to human-type sialic acid receptors, Current Opinion in Virology **60**, 101314 (2023).

[42] I. R. McNicholl and J. J. McNicholl, Neuraminidase inhibitors: zanamivir and oseltamivir, Annals of Pharmacotherapy **35**, 57 (2001).

[43] H. Kelly and B. J. Cowling, Influenza: the rational use of oseltamivir, The Lancet **385**, 1700 (2015).

[44] T. Jefferson and P. Doshi, Multisystem failure: the story of anti-influenza drugs, Bmj **348** (2014).

[45] A. T. Blanchard, A. S. Bazrafshan, J. Yi, J. T. Eisman, K. M. Yehl, T. Bian, A. Mugler, and K. Salaita, Highly polyvalent dna motors generate 100+ pn of force via autochemophoresis, Nano letters **19**, 6977 (2019).

[46] K. Yehl, A. Mugler, S. Vivek, Y. Liu, Y. Zhang, M. Fan, E. R. Weeks, and K. Salaita, High-speed dna-based rolling motors powered by rnase h, Nature nanotechnology **11**, 184 (2016).

[47] S. Kovacic, L. Samii, P. M. Curmi, H. Linke, M. J. Zuckermann, and N. R. Forde, Design and construction of the lawnmower, an artificial burnt-bridges motor, IEEE Transactions on NanoBioscience **14**, 305 (2015).

[48] I. N. Unksov, C. S. Korosec, P. Surendiran, D. Verardo, R. Lyttleton, N. R. Forde, and H. Linke, Through the eyes of creators: observing artificial molecular motors, ACS nanoscience Au **2**, 140 (2022).

[49] C. S. Korosec, I. N. Unksov, P. Surendiran, R. Lyttleton, P. M. Curmi, C. N. Angstmann, R. Eichhorn, H. Linke, and N. R. Forde, Motility of an autonomous protein-based artificial motor that operates via a burnt-bridge principle, Nature Communications **15**, 1511 (2024).